PHYSICAL REVIEW B **106**, 214412 (2022)

Low-energy magnon excitations and emerging anisotropic nature of short-range order in CrI_3

M. Jonak,[1] E. Walendy,[1] J. Arneth,[1] M. Abdel-Hafiez,[2] and R. Klingeler[1,*]
[1]*Kirchhoff Institute for Physics, Heidelberg University, INF 227, D-69120 Heidelberg, Germany*
[2]*Department of Physics and Astronomy, Uppsala University, Box 516, SE-751 20 Uppsala, Sweden*

(Received 25 March 2022; revised 13 October 2022; accepted 17 November 2022; published 9 December 2022)

We report on the low-energy magnetic excitations and the evolution of local magnetic fields in CrI_3 in a broad frequency regime of 30–330 GHz and in magnetic fields up to 15 T. Modeling the magnon branches by means of a domain-based ferromagnetic resonance model provides the microscopic parameters describing the magnetic excitations in the two-dimensional ferromagnet. Our data reveal the anisotropy gap of $\Delta = 80$ GHz at 2 K, which remarkably remains finite at T_C and vanishes only above $T_\Delta \simeq 80$ K, i.e., for $T \gtrsim 1.3T_C$. Concomitantly, anisotropic local magnetic fields are probed by a shift of the resonance lines in the same temperature regime. Well above T_C, we detect short-range magnetic correlations up to 200 K. The observed changing nature of the short-range correlations at T_Δ confirms the importance of spin-orbit coupling for the evolution of long-range ferromagnetism which develops from magnetically anisotropic short-range order. In addition, our analysis of the macroscopic magnetization enables to estimate the number of correlated spins well above T_C as well as the in-plane magnetic correlation length ξ_{ab}.

DOI: 10.1103/PhysRevB.106.214412

I. INTRODUCTION

The exfoliable quasi-two-dimensional (quasi-2D) van-der-Waals semiconductor CrI_3 attracts much attention not only thanks to displaying rich fundamental phenomena, such as long-range ferromagnetic order in a monolayer [1], a mixed ferromagnetic-bulk/antiferromagnetic-surface state [2,3], or exotic high-pressure phases [4], but also because of its technologically relevant properties. In addition to the ferromagnetic semiconducting state, this especially involves a linear magnetoelectric effect in a bilayer [5] or spin-filter giant magnetoresistance [6–8]. The spontaneous symmetry breaking in the true 2D limit exemplifies the all-important role of magnetocrystalline anisotropy in CrI_3. The magnetocrystalline anisotropy in CrI_3 arises neither due to single-ion anisotropy, which is negligible owing to the first-order quenching of the orbital momentum, nor due to shape which favors planar anisotropy [9,10]. Instead, it is supposed to originate from spin-orbit coupling on the ligand iodine ions [9,10] which gives rise to strongly anisotropic exchange interactions and selects the crystallographic *c* axis as the easy magnetization axis [11]. The spin-excitation spectra feature a gap at the Dirac point [12,13] whose origin, and especially the significance of Dzyaloshinskii-Moriya (DM) and/or Kitaev interactions for it, are controversially discussed [9,13–16].

Crystallographically, each Cr^{3+} magnetic ion in CrI_3 is coordinated by edge-sharing octahedra of I^- ions, with the Cr^{3+} ions lying in a hexagonal arrangement spanning the crystallographic *ab* plane. Adjacent planes are coupled by weak, van-der-Waals forces [17]. Crystallizing in a monoclinic $C2/m$ structure at room temperature, the material undergoes a structural phase transition at $T_S \simeq 212$ K to a rhombohedral $R\bar{3}$ crystal structure [17]. Owing to the octahedral environment, the $3d$-orbital manifold splits into lower-lying threefold degenerate t_{2g} and higher-lying twofold degenerate e_g orbitals, with total $S = 3/2$ and first-order quenching of the orbital momentum [18]. At 61 K, bulk CrI_3 develops long-range ferromagnetic order [17].

Our reported high-frequency electron spin resonance (HF-ESR) and macroscopic magnetization data provide the microscopic parameters describing the magnetic excitations and prove the significance of magnetocrystalline anisotropy for the development of long-range ferromagnetic order in CrI_3. Concretely, our data reveal the temperature dependence of the anisotropy gap which remains finite at T_C and vanishes only above $T_\Delta \simeq 80$ K. While short-range magnetic correlations persist up to at least 160 K, their nature changes at T_Δ, thereby confirming the importance of magnetocrystalline anisotropy for the evolution of long-range ferromagnetism.

II. EXPERIMENT

High-frequency/high-field electron spin resonance measurements were performed in the frequency range 30 GHz $\leqslant \nu \leqslant$ 330 GHz in a transmission mode and Faraday configuration ($k_{MW} \perp B$), utilizing unpolarized light. The generation and detection of the microwave radiation was facilitated by means of a millimeter-wave-vector network analyzer from AB Millimetre. The measurements were performed in a magnetocryostat equipped with a 18-Tesla superconducting magnet and a variable temperature insert (VTI) temperature control operating in the range 1.7 K $\leqslant T \leqslant$ 300 K [19]. An approximately rectangularly shaped thin single crystal of dimensions 2.2(1) mm × 1.4(1) mm × 0.095(15) mm was fixed under an argon atmosphere with Kapton tape to the inside walls of a vacuum-sealing microwave-transparent PEEK sample holder. The sample holder was fixed into a homemade sample rod

---

[*] klingeler@kip.uni-heidelberg.de

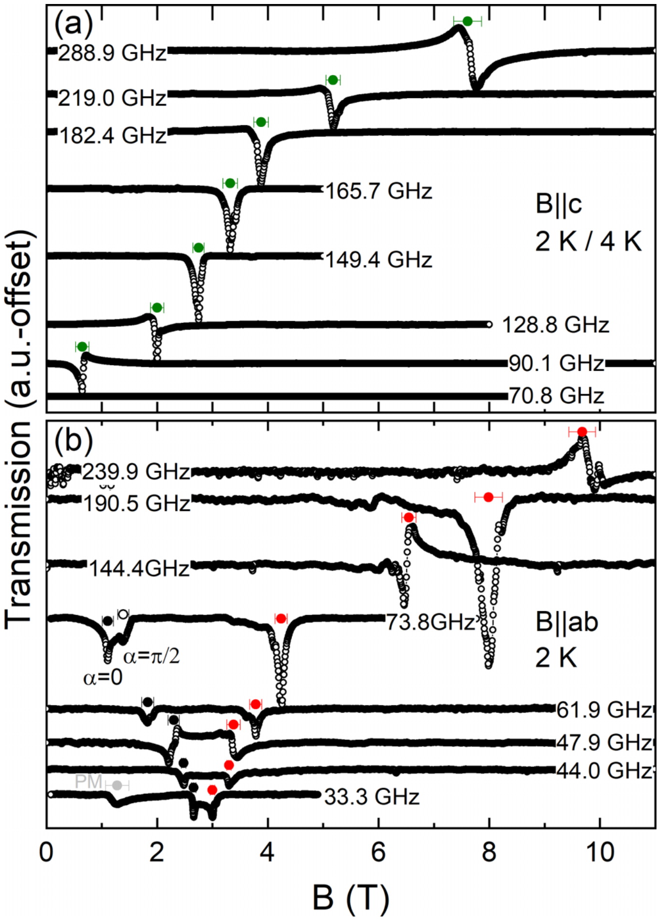

FIG. 1. Selected spectra at various frequencies obtained well below T_C for (a) $B||c$ axis, and; (b) $B||ab$ plane. Colored symbols mark positions of the resonance features.

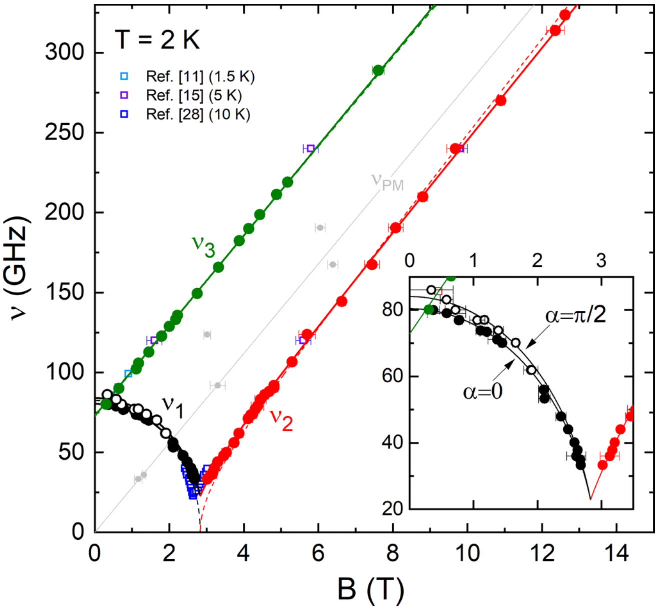

FIG. 2. Resonance-frequency–magnetic-field diagram of CrI_3 at 2 K. Data associated with branches $\nu_{1,2}$ were obtained for $B||ab$, ν_3 for $B||c$. Colors correspond to the symbols used in Fig. 1 to label the resonance features. Closed circles in branch ν_1 correspond to $\alpha = 0$, open circles to $\alpha = \pi/2$ (see text for details). Open square symbols show literature data (see legend). Solid lines display the fitting results based on a domain-based FMR model [Eqs. (1), (2), and (3)], dashed lines on a domain-free FMR model (see text for details). Light-grey solid line depicts a paramagnetic signal with $g = 2.00$. The inset zooms in on the low-frequency low-field region.

and installed into the magnetocryostat. In addition, isothermal magnetization measurements were performed using the vibrating sample magnetometer (VSM) option of the physical property measurement system (PPMS-14, Quantum Design). The magnetization measurements utilized a second, similarly shaped single-crystal piece with a mass of $m = 0.91$ mg. This too was mounted under an argon atmosphere, transferred in a vacuum-sealing container and installed into the PPMS in a minimum amount of time to avoid sample contamination. Both single-crystal pieces stemmed from the same batch obtained from HQ Graphene [20], which was characterized and studied in Ref. [21].

III. RESULTS

A. Field dependence of FMR modes

A selection of spectra obtained in the ferromagnetically ordered phase of CrI_3 with the external field applied along the *c* axis and within the *ab* plane, respectively, are displayed in Fig. 1. Several spectra in both crystallographic directions show a small amount of wave-phase mixing, resulting in asymmetric Lorentzian absorption peaks. Moreover, spectra obtained for $B||ab$ at $\nu \gtrsim 150$ GHz show an increased level of background noise. However, a careful comparison of the spectra obtained in the up- and down-sweep directions allows for an unambiguous assignment of all the resonance features (marked by colored symbols in Fig. 1). Whereas for the $B||c$ axis a single resonance feature is detected at all frequencies above 80 GHz, at least two distinct features are detected for $\nu < 90$ GHz for the $B||ab$ plane. Additionally, for 60 GHz $< \nu <$ 90 GHz the lower-field resonance feature splits into two distinct features, as highlighted by the closed and open circles in the spectrograph at $\nu = 73.8$ GHz in Fig. 1(b). Beyond the dominant features, a small number of spectra stemming from both orientations exhibit resonances which are not associated with the main branches [see, e.g., the low-field feature at $\nu = 33.3$ GHz for $B||ab$ in Fig. 1(b) marked by a grey circle and indicating a paramagnetic signal with $g = 2.00$].

All the low-temperature resonances are summarized in the resonance-frequency–magnetic-field diagram depicted in Fig. 2. To model the observed ferromagnetic resonance (FMR), the *c*-axis-oriented uniaxial magnetocrystalline anisotropy and the presence of domains spanning individual *ab* planes in CrI_3 are recalled [11,22]. Under the given constraints and for a Faraday configuration, the following set of equations describe the FMR behavior [23,24]:

$$\left(\frac{\nu_1}{\gamma_{\mathrm{ab}}}\right)^2 = (B_{\mathrm{A}} + N_x M_{\mathrm{S}})(B_{\mathrm{A}} + M_{\mathrm{S}}\sin^2\alpha) - \frac{(B_{\mathrm{A}} + M_{\mathrm{S}}\sin^2\alpha - N_z M_{\mathrm{S}})(B_{\mathrm{A}} + N_x M_{\mathrm{S}})}{(B_{\mathrm{A}} + N_y M_{\mathrm{S}})^2} B^2 \tag{1}$$

for the external magnetic field $B \leqslant B_A + N_y M_S$ applied within the *ab* plane;

$$\left(\frac{\nu_2}{\gamma_{ab}}\right)^2 = \{B - [B_A - (N_z - N_y)M_S]\}\{B - (N_y - N_x)M_S\} \tag{2}$$

for $B \geqslant B_A + N_y M_S$ applied within the *ab* plane and;

$$\frac{\nu_3}{\gamma_c} = B + B_A - N_z M_S \tag{3}$$

for B applied along the magnetic easy c axis.

In the above, B_A is the effective anisotropy field, M_S is the saturation magnetization, $\gamma_i = g_i \times 13.996$ (GHz T^{-1}) is the axial gyromagnetic ratio with the corresponding g-factor, and N_x, N_y, and N_z are the demagnetization factors of the macroscopic sample. α corresponds to the angle which the applied magnetic field B encloses with the magnetization direction of a particular domain. Fitting the detected ferromagnetic resonances by means of Eqs. (1) to (3) yields the following fitting parameters [25]: $B_A = 2.81(10)$ T; $M_S = 0.26(10)$ T; $g_{ab} = 2.04(4)$; $g_c = 2.01(1)$. The obtained anisotropy field compares well with its determination from magnetization studies [17,26,27]. Our analysis yields the saturation magnetization of 3.0(10) μ_B/f.u., which is in a good agreement with the theoretical expectations and also with previous magnetization measurements [17,26]. The magnon branches in the full frequency regime 30 to 330 GHz presented here correspond well to earlier FMR measurements obtained for $B||c$ at a few selected frequencies $\nu = 86$, 91 and 99 GHz at 1.5 K [11], and $\nu = 120$ and 240 GHz at 5 K [15], as well as for $B||ab$ in a narrow frequency window from 20 to 40 GHz at 10 K [28] (see the various open square symbols in Fig. 2). A small shift of the saturation field in the latter data with respect to the here-presented two-Kelvin data towards lower fields is observed, confirming that with increasing temperature the anisotropy field diminishes.

The experimental data are very well described by the domain-based model in Eqs. (1) to (3). The obtained FMR branches especially involve a strong bending of the softening magnon branch ν_1 when approaching the saturation field $B_{sat} \simeq 2.8$ T. We also emphasize that the finite gap remaining in this field region is correctly captured by the domain-based model. In contrast and for comparative purposes, Fig. 2 also includes fitting results from a tentative attempt to describe the resonance features in CrI$_3$ by means of a domain-free FMR model [29] (dashed lines). As is apparent, a better-fitting quality, with a seven-times-smaller residual-squares sum, is obtained in the framework of the domain-based model as compared to the domain-free picture. Moreover, the domain-free model predicts a complete closing of the gap at B_{sat}, which is not seen in the experimental data. Hence, our results corroborate the previous observation of domains in CrI$_3$ by means of microscopic methods [1,22,30].

The presence of domains is further established from our data by the observation of the splitting of the low-field resonance feature in the *ab* plane orientation, as demonstrated in Fig. 1(b) at $\nu = 73.8$ GHz. In the domain-based FMR model, these two features may be assigned to two extremal orientations of the domain walls with respect to the applied magnetic field: the more intense, lower-field feature corresponds to the parallel alignment of the domain walls with respect to the magnetic field $\alpha = 0$; the weaker, higher-field feature to the perpendicular alignment $\alpha = \pi/2$. The trend in intensity of the two features seen in Fig. 1(b) indicates that the domains are predominately oriented along the direction of the applied field. The observed difference of $\simeq 3.6$ GHz in the zero-field splitting between the two extremal orientations, $\alpha = 0$ and $\alpha = \pi/2$, may be considered as an estimate of the in-plane anisotropy energy.

An extension to the domain-based model presented above would be to treat the individual ferromagnetic domains not as merely randomly oriented with respect to each other, but as arranged in a periodic stripe fashion [31,32]. Figure S3 in the Supplemental Material (SM) visualizes the two possible scenarios of the domains' arrangement [33]. The effect of periodicity alters the resonance matrix and hence the field dependence of the resonance frequencies. Such a model was already used to describe the *ab* plane ferromagnetic resonance in CrI$_3$ in a limited frequency range [28]. However, for systems in which the sample thickness d is much greater than the domain width L such that the aspect ratio L/d becomes very small, the stripe-domain model reduces to the domain model presented in Eqs. (1) to (3). With the estimated domain width in CrI$_3$ in the order of 1 μm [22] and with the sample thickness in the range of 50 to 100 μm, neither the FMR branches presented at hand nor those in Ref. [28] are appreciably affected by the additional complexity due to the stripe-domain behavior. Moreover, micromagnetic simulations based on the stripe-domain model did not confirm the presence of stripe domains in CrI$_3$ [28].

B. Temperature dependence of Δ and evolution of quasistatic local fields

The temperature effect on the zero-field excitation gap is depicted in Fig. 3(a). To obtain these values, resonance-frequency–magnetic-field diagrams for $B||c$ were constructed at various temperatures and the field dependence of the resonance features fitted by means of Eq. (3) (see Fig. S4 in the SM [33]). The gap resulting from the $B||c$ data is labeled $\tilde{\Delta}_c$. At $T = 2$ K, an analogous procedure was applied also for the spectra obtained for $B||ab$. For higher temperatures, owing to the flat slope of the resonance branch ν_1 as $B \to 0$ T, $\tilde{\Delta}_{ab}$ was determined by following the shift and eventual disappearance of the corresponding low-field *ab* plane resonance feature belonging to ν_1.

The thus-obtained $\tilde{\Delta}_c$ and $\tilde{\Delta}_{ab}$ show a small difference between each other up to about 50 K, which can be attributed to demagnetization effects in the thin ferromagnetic sample (see Fig. S5 in the SM [33]). Correcting the gap values for demagnetization effects results in a vanishing difference in the gap sizes within the error bars, thus confirming a single anisotropy gap, which amounts to $\Delta = 80(1)$ GHz at 2 K [see Fig. 3(a)] [34].

Notably, determining the field dependence of the resonance branches in a large frequency regime enables us to follow the zero-field anisotropy gap above T_C. We emphasize that the presence as well as the approximate size of the gap and its temperature evolution can be directly read off from the data by following the linear field dependence of the resonance features

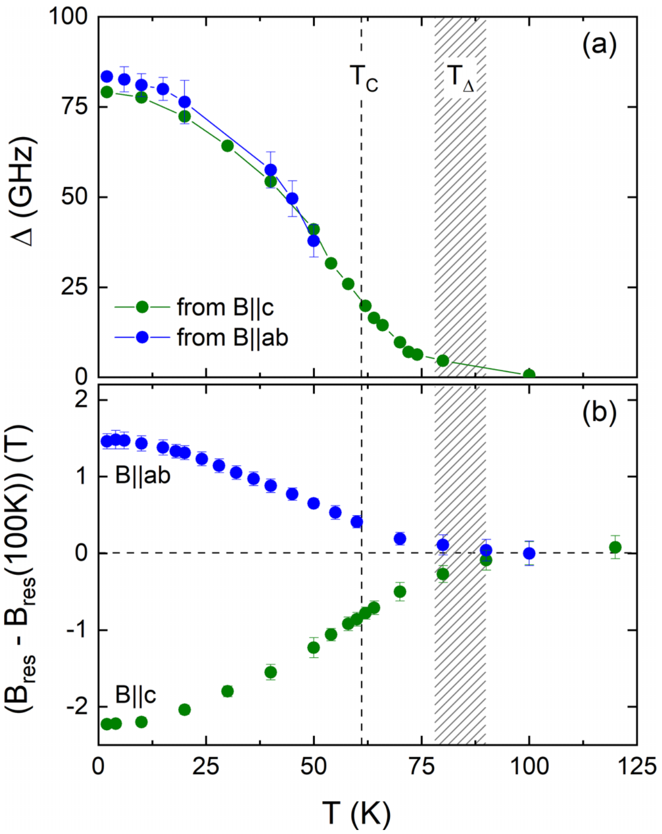

FIG. 3. (a) Temperature dependence of the zero-field excitation gap from measurements for $B||c$ axis (green circles) and $B||ab$ plane (blue circles). For comparison with literature data obtained by inelastic neutron scattering from Ref. [13] see Fig. S6 in the Supplemental Material [33]. (b) Difference of resonance fields at $\nu = 135.7$ GHz ($B||c$ axis, green circles) and $\nu = 73.8$ GHz ($B||ab$ plane, blue circles) from their respective value at 100 K. Vertical dashed line marks T_C, horizontal dashed line in (b) the position of a zero resonance-field shift, and shaded area shows the region around T_Δ where the gap vanishes.

predicted by Eq. (3), while demagnetization correction yields only small shifts. The size of the correction vanishes with increasing temperature, and, in particular, no correction was applied for $T > T_C$. As shown in Fig. 3(a), our experiment reveals that at 62 K (i.e. just above T_C) Δ amounts to 19.8(7) GHz (approximately 25% of its value at 2 K) and vanishes only for $T \gtrsim 80$ K, i.e., for $T \gtrsim 1.3T_C$. The approximate region for which the anisotropy gap vanishes is designated by T_Δ (see the shaded area in Fig. 3). We note that the resonant features for $B||c$ exhibit a linear behavior in the entire region of accessed frequencies and fields at each temperature (cf. Fig. S4 in the SM [33]). In order for the value of Δ to vanish at any $T \leqslant T_\Delta$, the corresponding resonance branch would have to bend to lower frequencies as $B \rightarrow 0$ T. However, such a bending is neither observed in the experimentally accessible frequency range nor consistent with the predictions for the ordered ferromagnetic state [cf. Eq. (3)] or for a paramagnetic regime ($\nu_{PM} = g\mu_B B/h$).

The appearance of a finite gap is accompanied by the presence of quasistatic local magnetic fields detected by our HF-ESR experiment. Generally, the evolution of local magnetic fields upon cooling is signalled by the shift of the resonance fields from their paramagnetic value [35]. Approximating the paramagnetic resonance field by its value at 100 K, above which the paramagnetic resonance signal was not detected in our experiment, yields a resonance shift shown in Fig. 3(b). Below 80 K, which corresponds to the temperature T_Δ, the resonance positions shift towards higher values in the case of $B||ab$, while the opposite trend appears for $B||c$. These observations imply the presence of local anisotropic magnetic fields in this temperature regime, which are quasistatic on the timescale of the microwave experiment. The anisotropic nature of the observed resonance shift correlates with the observation of the finite anisotropy gap in this temperature regime, while neither Δ nor the quasistatic local fields exhibit visible discontinuities at T_C. The sign of the shift opposes the shift in $CrCl_3$ [35], which, however, exhibits planar anisotropy, and is similar to what is found in the uniaxial system $Cr_2Ge_2Te_6$ [36]. The present data show that the effective magnetic easy axis in CrI_3 is oriented parallel to the crystallographic c axis, as is also suggested by the low-temperature magnon field dependence presented above and by static magnetization measurements [17,26].

C. Linewidth and slope of the resonance branches

The temperature evolution of the width of the resonances is deduced from measurements at a fixed resonance frequency. The temperature dependence of spectra obtained at $\nu = 102.1$ GHz for $B||c$ axis is displayed in Fig. 4(a). The spectra exhibit an approximately symmetric Lorentzian resonance feature which broadens and shifts to higher resonance fields with increasing temperature. A similar behavior all the way up to 120 K is found for $B||c$ also at $\nu = 135.7$ GHz (data not shown). Fitting the spectra by means of a Lorentzian function [red solid lines in Fig. 4(a)] yields the temperature dependence of the linewidth ΔB, quantified as the function's half width at half maximum. As can be seen in Fig. 4(b), the linewidth shows two regions of distinct temperature dependence, demarcated by the ferromagnetic ordering temperature. The weak temperature dependence of ΔB in the ferromagnetically ordered phase suggests that magnetization relaxation in this temperature region is dominated by a spin-spin relaxation process [37]. At the lowest temperature, the linewidth amounts to $\Delta B \simeq 50$ mT. This corresponds to the relaxation time on the order of $\simeq 10^{-10}$ s, which is typical for spin-spin relaxation processes in long-range-ordered ferromagnets [38,39].

A much more pronounced, approximately linear temperature dependence of the linewidth is observed for $T > T_C$. Although vanishing of the resonance feature restricts the accessible temperature regime to $T \leqslant 100$ K, the data do not indicate any changes associated with T_Δ. The distinct increase of the linewidth for $T > T_C$ indicates the gradual prevalence of a spin-phonon relaxation mechanism in this temperature regime [40]. It was previously argued that an increase in ΔB for $T \gg T_C$ can be due to a temperature-dependent phonon modulation either of the antisymmetric exchange interaction or of the crystalline field [40]. Whereas a phonon modulation of the crystalline field was argued as the appropriate relaxation path in the related van der Waals feromagnet

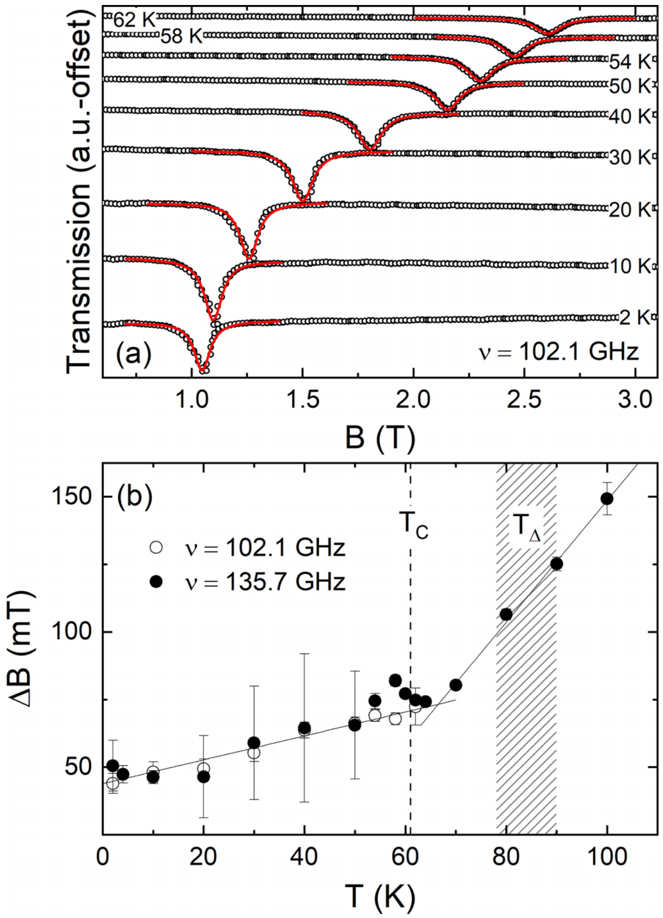

FIG. 4. (a) $B||c$ axis spectra at $\nu = 102.1$ GHz and various temperatures (black), fitted by means of a Lorentzian function (red). (b) Corresponding linewidth, ΔB, obtained from spectra measured at $\nu = 102.1$ GHz and $\nu = 135.7$ GHz. Lines show linear fits to the data as a guide for the eye. Vertical dashed line marks the ferromagnetic ordering temperature, shaded area marks the temperature region T_Δ in which the anisotropic effects vanish (cf. Fig. 3).

CrBr$_3$ [40]; both of the above scenarios are possible in CrI$_3$. In particular, in several studies the antisymmetric, DM exchange interactions were seen as essential for opening of the topological Dirac gap [12,14,41], but alternative accounts were also proposed [9,15,16].

Finally, we discuss the slope of the $B||c$ resonance branches which are linear in the whole temperature regime and hence can be used to deduce the g-factor as described by Eq. (3). Analyzing the spectra shown in Fig. S4 of the SM [33] accordingly yields the effective g-factor, g_c, displayed in Fig. 5. It essentially describes the slope of the magnon branches of our measurements. At 2 K, it amounts to $g_c = 2.01(1)$, which agrees with the paramagnetic spectroscopic value [18,42]. Upon heating, g_c increases up to T_C and beyond, reaching a plateau maximum with a peak value of 2.30(2) in the temperature region between 64 K and 74 K. Eventually, g_c decreases for $T > 74$ K, amounting to $g_c = 2.19(3)$ at $T = 100$ K. A similar analysis of high-temperature HF-ESR data to obtain the g-factor was previously performed for CrGeTe$_3$ [24,43] and CrSiTe$_3$ [24]. In both systems, a comparable increase in the g-factor for the field applied along the easy magnetization axis was observed up to T_C. In Ref. [24] the evolution of the g-factor was followed also for $T > T_C$, and a decrease of g_c was found, albeit with no plateau regime as observed for CrI$_3$ (see Fig. 5). It was argued that on-site as well as off-site spin-orbit coupling [43], or anisotropic symmetric exchange and single-ion anisotropy [24], respectively, are responsible for the observed temperature dependence of the g-factor.

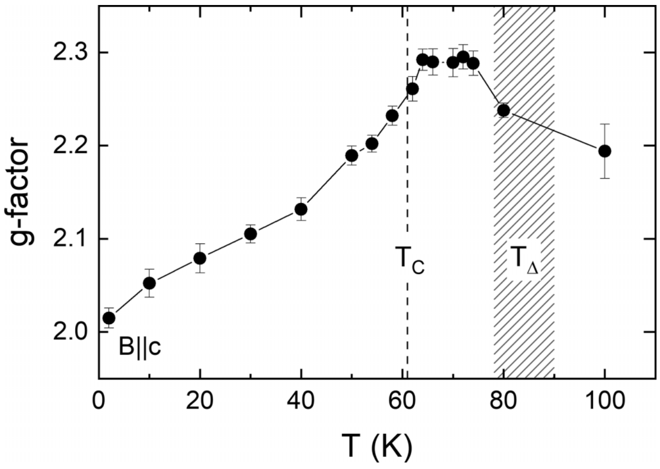

FIG. 5. Temperature dependence of the effective g-factor obtained from the slope of the resonance-frequency–magnetic-field diagrams obtained for $B||c$ axis (see the text) at various temperatures depicted in Fig. S4 in the Supplemental Material. Vertical dashed line marks the ferromagnetic ordering temperature, shaded area marks the temperature region T_Δ in which the anisotropic effects vanish (cf. Fig. 3).

D. High-temperature isothermal magnetization

Figure 6(a) presents isothermal magnetization obtained in a range of temperatures above T_C. To illustrate the anisotropic behavior, the data for $B||c$ (green solid lines) were normalized by $M(B||ab)$ (black solid lines) at $B = 14$ T. The scaled curves indicate that a sizable difference exists between the c axis and ab plane magnetization at temperatures up to $\simeq 100$ K. To visualize this behavior, the difference $M_c - M_{ab}$ at 1 T is shown in Fig. 6(b). It can be seen that in the temperature regime in which the HF-ESR data exhibit local anisotropic fields and a finite anisotropy gap the static magnetization also exhibits an anisotropic magnetic response to the applied magnetic field along the two principal orientations. In the ordered phase, the difference in the saturation fields $B_c^{\mathrm{sat}} - B_{ab}^{\mathrm{sat}}$ directly measures the anisotropy field B_A in Eqs. (1) to (3) and is hence directly related to Δ deduced from HF-ESR. If $\Delta \neq 0$, $M_c - M_{ab}$ is also finite at lower fields. Therefore, the observed magnetization anisotropy above T_C agrees with the presence of a finite gap above T_C.

The magnetization curves in Fig. 6(a) exhibit a right bending in the magnetic field even at temperatures for which the anisotropy is lifted and up to the highest measured temperature $T = 200$ K. Whereas in a purely paramagnetic system the magnetization curves in the studied field regime would be perfectly linear, the observed bending implies the presence of ferromagnetic correlations which in a ferromagnetic material might be field-induced. Motivated by the description of the

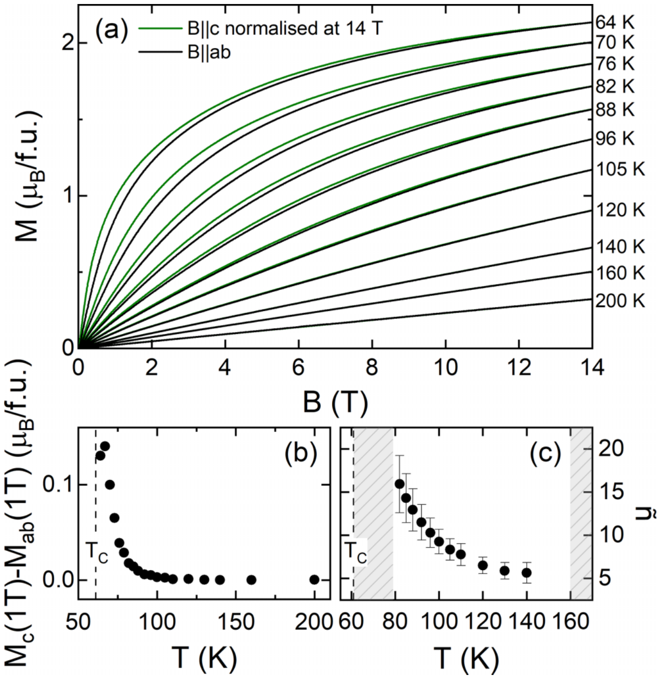

FIG. 6. (a) Isothermal magnetization at selected temperatures as a function of $B||ab$ plane (black), and of $B||c$ (green) scaled by M_{ab}(14 T) for each respective temperature. (b) Difference in magnetization for $B||c$ and $B||ab$ at 1 T. (c) Temperature dependence of the number of ferromagnetically correlated moments $\tilde{n}$ (see the text). Shaded areas mark temperature regions for which no reliable estimate of $\tilde{n}$ is possible. Vertical dashed lines mark the long-range ferromagnetic ordering temperature.

magnetoresistance in the inhomogeneous paramagnetic phase of ferromagnetic manganites [44], the magnetization curves for $B||ab$ in Fig. 6(a) are fitted by a modified Brillouin function $B_{\tilde{S}}$ with a field-independent magnetic moment $\tilde{S}$:

$$M = M_s B_{\tilde{S}}\left(\frac{g\mu_B \tilde{S} B}{k_B T}\right) + \chi_0 B. \tag{4}$$

Here, M_S is the saturation magnetization of the ferromagnetically correlated ensemble, χ_0 a field-independent contribution to the susceptibility, $g = 2$ is the g-factor, μ_B the Bohr magneton, and k_B the Boltzmann constant. The fits at selected temperatures are displayed in Fig. S7 of the SM [33]. While the data just above T_C are not captured well by Eq. (4), the fits employing a fixed magnetic moment describe the experimental data very well for $T \geqslant 80$ K. [45]. This result suggests that the observed curvature signals the field-driven alignment of short-range ferromagnetically correlated spin ensembles whose total moments do not appreciably depend on the external field. The observation of a negligible effect of the field on the spin-ensemble size above around 80 K agrees with the rather weakly field-dependent crossover temperature from para to ferromagnetism in the magnetic phase diagram of CrI_3 [3]. Based on Raman studies it was concluded that the crossover temperature increases linearly by approximately 10 K in $B = 7$ T.

The obtained $\tilde{S}$ may be used to asses the number of ferromagnetically correlated Cr^{3+} moments, $\tilde{n} = \tilde{S}/S$, with $S = 3/2$ (cf. Ref. [44]). This is plotted in Fig. 6(c). With increasing temperature $\tilde{n}$ decreases, indicating the decrease of correlations. In an attempt to obtain a rough estimate of the ferromagnetic correlation length ξ_{ab}, motivated by recent experimental [12,13,15] and theoretical [21,46,47] studies we assume a 2D model. Here, the ensembles of $\tilde{n}$ correlated spins span isotropically the *ab* plane such that ξ_{ab} may be expressed as $\xi_{ab} = \sqrt{(2\sqrt{3}a^2/\pi)\cdot\tilde{S}}$ (cf. Ref. [48]), with $a = 3.965$ Å being the in-plane nearest-neighbor chromium-chromium distance [17]. Our analysis yields $\xi_{ab} \simeq 15$ Å at 100 K ($T/T_C \simeq 1.6$). This result may be compared to the recent inelastic neutron scattering (INS) on the related van der Waals ferromagnet $CrSiTe_3$ where the 2D nature of spin correlations is observed above $T_C = 33$ K and up to room temperature, with $\xi_{ab} \simeq 9$ Å at 55 K (i.e., at similar T/T_C) [49].

IV. DISCUSSION AND CONCLUSION

In a wide frequency and magnetic-field regime, low-energy magnon excitations in CrI_3 are exactly captured by a domain-based model in Eqs. (1) to (3). The analysis by means of this model provides microscopic parameters from which the magnetic easy axis, the anisotropy gap at $B = 0$ T, and the axis-dependent g-factors are obtained. The experimental spectra also provide information on the local magnetic fields probed by the Cr^{3+} moments and on the linewidth. Quantitatively, our analysis yields an anisotropy gap of $\Delta = 80(1)$ GHz at $T = 2$ K [see Fig. 3(a)]. Using only a few measurement frequencies or a rotation of the crystal, previous FMR studies reported gap sizes of $\Delta = 82.9$ GHz [11] and $\Delta = 72.5$ GHz [15], respectively. INS experiments, which exhibit a lower-energy resolution than the FMR data at hand, found $\Delta = 90(4)$ GHz [13].

In the long-range-ordered phase, the temperature dependence of the anisotropy gap [Fig. 3(a)] corresponds to the recent observations by means of INS [13]. Our experimental results, however, reveal that $\Delta(T)$ is finite at T_C and does not exhibit any detectable anomaly at the ferromagnetic ordering temperature. Just above T_C, Δ amounts to $\simeq 25$ % of its value at 2 K and vanishes only above $T_\Delta \simeq 1.3T_C$. The finite value of the anisotropy gap at T_C contrasts with the observation of its vanishing by INS [13] (see also Fig. S6 in the SM [33]). The presence of anisotropic local magnetic fields below T_Δ is confirmed by the corresponding shifts in the resonance fields [see Fig. 3(b)], which unambiguously prove the presence of quasistatic local magnetic fields. These results are corroborated by static magnetization since an anisotropic response of the spins to an external magnetic field up to $\simeq 100$ K is also observed in isothermal magnetization [Figs. 6(a) and 6(b)].

At the same time, the finite right bending of the isothermal magnetization above T_C and up to 200 K indicates short-range ferromagnetic correlations in this temperature regime. Such a behavior is expected in a short-range ferromagnetically ordered regime which in CrI_3 extends up to at least 150 K, as shown by recent specific heat measurements [50,51]. The fact that isothermal magnetization well above T_C is described by a modified Brillouin function with a fixed magnetic moment suggests that the observed right bending can be employed to estimate the number of correlated moments and — when further assuming a 2D nature of the correlations — of the in-plane correlation length ξ_{ab}.

Overall, our results demonstrate the presence of three distinct temperature regimes in addition to the high-temperature paramagnetic regime above $\simeq 200$ K. At $T_\Delta \leqslant T \lesssim 200$ K, the system exhibits short-range magnetic order, which involves neither a finite zero-field excitation gap nor anisotropic local magnetic fields. Upon cooling below T_Δ, the short-range order is associated with both, a finite excitation gap and the presence of an anisotropic shift in the resonance fields, while at last long-range order develops at T_{C}. Hence, our data imply a scenario of a purely Heisenberg-like (i.e., isotropic) short-range order at $T_\Delta \leqslant T \lesssim 200$ K, which develops an anisotropic character below T_Δ. In particular, our findings experimentally confirm that long-range order does not evolve from a purely Heisenberg-like short-range-ordered regime through increasing in-plane correlations in the presence of a small but finite interplanar coupling as observed, e.g., in the paradigmatic 2D Heisenberg system La_2CuO_4 [52]. Instead, the onset of anisotropic effects well above T_{C} found in our study indicates that long-range ferromagnetic order in CrI_3 is at least partly driven by magnetocrystalline anisotropy, as also suggested previously by theoretical studies [9,46] and by the observation of long-range order in a monolayer of CrI_3 [1].

ACKNOWLEDGMENTS

We would like to thank A. Alfonsov, V. Kataev, and M. Haverkort for fruitful discussions. Financial support by BMBF via the project SpinFun (13XP5088) and by Deutsche Forschungsgemeinschaft (DFG) under Germany's Excellence Strategy EXC2181/1-390900948 (the Heidelberg STRUCTURES Excellence Cluster) and through project KL 1824/13-1 is gratefully acknowledged. We also acknowledge support by the European Union's Horizon 2020 Research and Innovation Programme, under Grant No. 824109 (European Microkelvin Platform). M.A.-H. acknowledges the financial support from the Swedish Research Council (VR) under the Project No. 2018-05393.

---

[1] B. Huang, G. Clark, E. Navarro-Moratalla, D. R. Klein, R. Cheng, K. L. Seyler, D. Zhong, E. Schmidgall, M. A. McGuire, D. H. Cobden, W. Yao, D. Xiao, P. Jarillo-Herrero, and X. Xu, Nature (London) **546**, 270 (2017).

[2] B. Niu, T. Su, B. A. Francisco, S. Ghosh, F. Kargar, X. Huang, M. Lohmann, J. Li, Y. Xu, T. Taniguchi, K. Watanabe, D. Wu, A. Balandin, J. Shi, and Y.-T. Cui, Nano Lett. **20**, 553 (2020).

[3] S. Li, Z. Ye, X. Luo, G. Ye, H. H. Kim, B. Yang, S. Tian, C. Li, H. Lei, A. W. Tsen, K. Sun, R. He, and L. Zhao, Phys. Rev. X **10**, 011075 (2020).

[4] A. Ghosh, D. Singh, T. Aramaki, Q. Mu, V. Borisov, Y. Kvashnin, G. Haider, M. Jonak, D. Chareev, S. A. Medvedev, R. Klingeler, M. Mito, E. H. Abdul-Hafidh, J. Vejpravova, M. Kalbàč, R. Ahuja, O. Eriksson, and M. Abdel-Hafiez, Phys. Rev. B **105**, L081104 (2022).

[5] S. Jiang, J. Shan, and K. F. Mak, Nat. Mater. **17**, 406 (2018).

[6] T. Song, X. Cai, M. W.-Y. Tu, X. Zhang, B. Huang, N. P. Wilson, K. L. Seyler, L. Zhu, T. Taniguchi, K. Watanabe, M. A. McGuire, D. H. Cobden, D. Xiao, W. Yao, and X. Xu, Science **360**, 1214 (2018).

[7] Z. Wang, I. Gutiérrez-Lezama, N. Ubrig, M. Kroner, M. Gibertini, T. Taniguchi, K. Watanabe, A. Imamoğlu, E. Giannini, and A. F. Morpurgo, Nat. Commun. **9**, 2516 (2018).

[8] H. H. Kim, B. Yang, T. Patel, F. Sfigakis, C. Li, S. Tian, H. Lei, and A. W. Tsen, Nano Lett. **18**, 4885 (2018).

[9] J. L. Lado and J. Fernández-Rossier, 2D Mater. **4**, 035002 (2017).

[10] D.-H. Kim, K. Kim, K.-T. Ko, J. H. Seo, J. S. Kim, T.-H. Jang, Y. Kim, J.-Y. Kim, S.-W. Cheong, and J.-H. Park, Phys. Rev. Lett. **122**, 207201 (2019).

[11] J. F. Dillon and C. E. Olson, J. Appl. Phys. **36**, 1259 (1965).

[12] L. Chen, J.-H. Chung, M. B. Stone, A. I. Kolesnikov, B. Winn, V. O. Garlea, D. L. Abernathy, B. Gao, M. Augustin, E. J. G. Santos, and P. Dai, Phys. Rev. X **11**, 031047 (2021).

[13] L. Chen, J.-H. Chung, T. Chen, C. Duan, A. Schneidewind, I. Radelytskyi, D. J. Voneshen, R. A. Ewings, M. B. Stone, A. I. Kolesnikov, B. Winn, S. Chi, R. A. Mole, D. H. Yu, B. Gao, and P. Dai, Phys. Rev. B **101**, 134418 (2020).

[14] Y. O. Kvashnin, A. Bergman, A. I. Lichtenstein, and M. I. Katsnelson, Phys. Rev. B **102**, 115162 (2020).

[15] I. Lee, F. G. Utermohlen, D. Weber, K. Hwang, C. Zhang, J. van Tol, J. E. Goldberger, N. Trivedi, and P. C. Hammel, Phys. Rev. Lett. **124**, 017201 (2020).

[16] L. Ke and M. I. Katsnelson, npj Comput. Mater. **7**, 4 (2021).

[17] M. A. McGuire, H. Dixit, V. R. Cooper, and B. C. Sales, Chem. Mater. **27**, 612 (2015).

[18] A. Abragam and B. Bleaney, *Electron Paramagnetic Resonance of Transition Ions* (Oxford University Press, Oxford, 2012).

[19] P. Comba, M. Großhauser, R. Klingeler, C. Koo, Y. Lan, D. Müller, J. Park, A. Powell, M. J. Riley, and H. Wadepohl, Inorg. Chem. **54**, 11247 (2015).

[20] www.hqgraphene.com.

[21] J. Arneth, M. Jonak, S. Spachmann, M. Abdel-Hafiez, Y. O. Kvashnin, and R. Klingeler, Phys. Rev. B **105**, L060404 (2022).

[22] O. Bostanjoglo and W. Vieweger, Physica Status Solidi (b) **32**, 311 (1969).

[23] J. Smit and H. Beljers, Philips Research Technical Report No. **R263**, p. 113 (1955).

[24] Z. Li, D.-H. Xu, X. Li, H.-J. Liao, X. Xi, Y.-C. Yu, and W. Wang, Abnormal critical fluctuations revealed by magnetic resonance in the two-dimensional ferromagnetic insulators, arXiv:2101.02440.

[25] For the fits, the value of α in Eq. (1) was fixed to $\alpha = 0$ and $\alpha = \pi/2$, respectively, to account for the two *ab* plane low-field branches.

[26] N. Richter, D. Weber, F. Martin, N. Singh, U. Schwingenschlögl, B. V. Lotsch, and M. Kläui, Phys. Rev. Mater. **2**, 024004 (2018).

[27] A. Ghosh, H. J. M. Jönsson, D. J. Mukkattukavil, Y. Kvashnin, D. Phuyal, M. Agåaker, A. Nicolaou, M. Jonak, R. Klingeler, M. V. Kamalakar, R. Håkan, T. Sarkar, A. N. Vasiliev, S. Butorin, J.-E. Rubensson, O. Eriksson, and M. Abdel-Hafiez, arXiv:2201.04400.

[28] X. Shen, H. Chen, Y. Li, H. Xia, F. Zeng, J. Xu, H. Y. Kwon, Y. Ji, C. Won, W. Zhang, and Y. Wu, J. Magn. Magn. Mater. **528**, 167772 (2021).

[29] *Ferromagnetic Resonance*, edited by S.V. Vonsovskii (translated from Russian by Z. Lerman) (Israel Program for Scientific Translations, Jerusalem, 1964).

[30] L. Thiel, Z. Wang, M. A. Tschudin, D. Rohner, I. Gutiérrez-Lezama, N. Ubrig, M. Gibertini, E. Giannini, A. F. Morpurgo, and P. Maletinsky, Science **364**, 973 (2019).

[31] J. O. Artman and S. H. Charap, J. Appl. Phys. **49**, 1587 (1978).

[32] F. J. Rachford, P. Lubitz, and C. Vittoria, J. Appl. Phys. **53**, 8940 (1982).

[33] See Supplemental Material at http://link.aps.org/supplemental/10.1103/PhysRevB.106.214412 for details on schematics of the crystal structure and of the main magnetic exchange interactions, the visualization of potential magnetic domain patterns, additional resonance-frequency–magnetic-field diagrams at various temperatures, the temperature dependence of the obtained ESR anisotropy gap prior to demagnetization correction and its comparison to the literature values obtained by inelastic neutron scattering, as well as magnetization curves with corresponding fits.

[34] For instance, demagnetization corrections at 2 K shift $\tilde{\Delta}_\mathrm{c}$ by $+\gamma_\mathrm{c}N_zM_\mathrm{S} = 6.4$ GHz and $\tilde{\Delta}_\mathrm{ab}$ by $-\gamma_\mathrm{ab}N_xM_\mathrm{S} = -0.4$ GHz.

[35] J. Zeisner, K. Mehlawat, A. Alfonsov, M. Roslova, T. Doert, A. Isaeva, B. Büchner, and V. Kataev, Phys. Rev. Mater. **4**, 064406 (2020).

[36] J. Zeisner, A. Alfonsov, S. Selter, S. Aswartham, M. P. Ghimire, M. Richter, J. van den Brink, B. Büchner, and V. Kataev, Phys. Rev. B **99**, 165109 (2019).

[37] C. Kittel and E. Abrahams, Rev. Mod. Phys. **25**, 233 (1953).

[38] A. F. Kip and R. D. Arnold, Phys. Rev. **75**, 1556 (1949).

[39] D. W. Healy, Phys. Rev. **86**, 1009 (1952).

[40] D. Huber and M. Seehra, J. Phys. Chem. Solids **36**, 723 (1975).

[41] L. Chen, J.-H. Chung, B. Gao, T. Chen, M. B. Stone, A. I. Kolesnikov, Q. Huang, and P. Dai, Phys. Rev. X **8**, 041028 (2018).

[42] C. L. Saiz, M. A. McGuire, S. R. J. Hennadige, J. van Tol, and S. R. Singamaneni, MRS Advances **4**, 2169 (2019).

[43] S. Khan, C. W. Zollitsch, D. M. Arroo, H. Cheng, I. Verzhbitskiy, A. Sud, Y. P. Feng, G. Eda, and H. Kurebayashi, Phys. Rev. B **100**, 134437 (2019).

[44] P. Wagner, I. Gordon, L. Trappeniers, J. Vanacken, F. Herlach, V. V. Moshchalkov, and Y. Bruynseraede, Phys. Rev. Lett. **81**, 3980 (1998).

[45] Note that the very weak right bending for 160 K $\leqslant T \leqslant$ 200 K prevents reliable fitting in this temperature regime.

[46] O. Besbes, S. Nikolaev, N. Meskini, and I. Solovyev, Phys. Rev. B **99**, 104432 (2019).

[47] S. Feldkemper and W. Weber, Phys. Rev. B **57**, 7755 (1998).

[48] R. Klingeler, B. Büchner, S.-W. Cheong, and M. Hücker, Phys. Rev. B **72**, 104424 (2005).

[49] T. J. Williams, A. A. Aczel, M. D. Lumsden, S. E. Nagler, M. B. Stone, J.-Q. Yan, and D. Mandrus, Phys. Rev. B **92**, 144404 (2015).

[50] G. T. Lin, X. Luo, F. C. Chen, J. Yan, J. J. Gao, Y. Sun, W. Tong, P. Tong, W. J. Lu, Z. G. Sheng, W. H. Song, X. B. Zhu, and Y. P. Sun, Appl. Phys. Lett. **112**, 072405 (2018).

[51] K. Spurgeon, G. Kozlowski, M. A. Susner, Z. Turgut, and J. Boeckl, SCIREA J. Electric Engin. **5**, 141 (2020).

[52] S. J. Blundell, *Magnetism in Condensed Matter*, Oxford Master Series in Condensed Matter Physics (Oxford University Press, Oxford, 2001).